Tetragonal fcc-Fe induced by κ-carbide precipitates: Atomic scale insights from correlative electron microscopy, atom probe tomography, and density functional theory

Christian H. Liebscher,[1] Mengji Yao,[1] Poulumi Dey,[1] Marta Lipińska-Chwalek,[2,3] Benjamin Berkels,[4] Baptiste Gault,[1] Tilmann Hickel,[1] Michael Herbig,[1] Joachim Mayer,[2,3] Jörg Neugebauer,[1] Dierk Raabe,[1] Gerhard Dehm,[1] and Christina Scheu[1]

[1]*Max-Planck-Institut für Eisenforschung GmbH, 40237 Düsseldorf, Germany*

[2]*Central Facility for Electron Microscopy, RWTH Aachen University, 52074 Aachen, Germany*

[3]*Ernst Ruska-Centre (ER-C) for Microscopy and Spectroscopy with Electrons, Forschungszentrum Jülich GmbH, 52425 Jülich, Germany*

[4]*Aachen Institute for Advanced Study in Computational Engineering Science (AICES), RWTH Aachen University, 52062 Aachen, Germany*

(Received 5 September 2017; published 22 February 2018)

Correlative scanning transmission electron microscopy, atom probe tomography, and density functional theory calculations resolve the correlation between elastic strain fields and local impurity concentrations on the atomic scale. The correlative approach is applied to coherent interfaces in a κ-carbide strengthened low-density steel and establishes a tetragonal distortion of fcc-Fe. An interfacial roughness of ~1 nm and a localized carbon concentration gradient extending over ~2–3 nm is revealed, which originates from the mechano-chemical coupling between local strain and composition.

DOI: 10.1103/PhysRevMaterials.2.023804

I. INTRODUCTION

Designing internal phase boundaries has become a highly successful strategy to develop structural and functional materials with superior mechanical or electronic properties [1,2]. A challenge in designing such materials s, that fundamental mechanisms on the coupling of elastic and chemical effects at interfaces remain elusive, even when applying modern characterization techniques. The dispersion of nanometer-scale coherent precipitates in a solid solution, for example, is an effective way to design materials with outstanding mechanical properties even at high temperatures where classical mechanisms, such as solid-solution hardening, fail [3]. Complex internal stress states develop around and in between these nano-precipitates that affect the interaction with dislocations, the elastic self-interaction, and local chemical equilibrium [4–8].

Powerful metrological techniques to resolve atomic scale compositional fluctuations at interfaces in complex materials are high resolution transmission electron microscopy (TEM) and atom probe tomography (APT) [9,10]. Despite the enormous progress made over the past decades in improving their spatial and elemental resolution, both techniques suffer from limitations that restrict their capabilities to resolve structural and compositional features individually. Correlative approaches, that combine experimental techniques with *ab initio* simulations can overcome the limitations of a single technique, but require the development of new strategies to spatially align sample features on a nanometer or even atomistic scale.

Aberration-corrected scanning TEM (STEM) enables one to resolve complex materials with atomic resolution, and, when a convergent beam is scanned over the sample, the image intensity is directly proportional to the mean atomic number [11]. The precision to locate atomic columns in STEM micrographs was shown to be in the picometer range, giving access to atomic column displacements, local crystallography, and composition [9,12–14]. The detection of light elements, such as carbon (C) and oxygen (O), still remains challenging in STEM due to their low interaction with the electron beam. Aberration correction increased the chemical sensitivity of spectroscopic techniques to below 0.1 at. %, but it strongly depends on the sample geometry, and highest sensitivity is only obtainable with a loss in spatial resolution [9]. An ideal technique to correlate with STEM is APT, that not only can detect elements down to hydrogen (H), but also gives access to the three-dimensional (3D) elemental distribution within the specimen. APT provides the highest elemental sensitivity, but the anomalous field evaporation behavior and local magnifications at or near interfaces induce aberrations in the ion trajectories that alter the precision of the 3D reconstruction [15]. The correlation of (S)TEM and APT is a way to overcome the limitations of both techniques and has been established on a variety of material systems [16–20]. Nevertheless, *ab initio* calculations are required to explore the atomistic origins of local chemical equilibrium. Density functional theory (DFT) approaches in combination with thermodynamic concepts have successfully been applied to complex, interface dominated materials to unravel elastic and magnetic effects on phase stability [21,22].

In this work, we show how atomic resolution STEM, APT, and DFT can be correlated and are able to resolve elemental distributions, elastic strain fields, and their relationship on the nanometer scale. The power of the presented threefold correlative approach is demonstrated on interfaces in a nano-precipitation hardened, low-density steel. The atomic scale structural information from STEM is used to calibrate the APT reconstruction (see Fig. 1). The refined compositional information from APT, in particular the concentration of interstitial C atoms, is an essential component for the *ab initio* simulations to fully explore the connection of local lattice distortions on the C solubility. In return, the computations

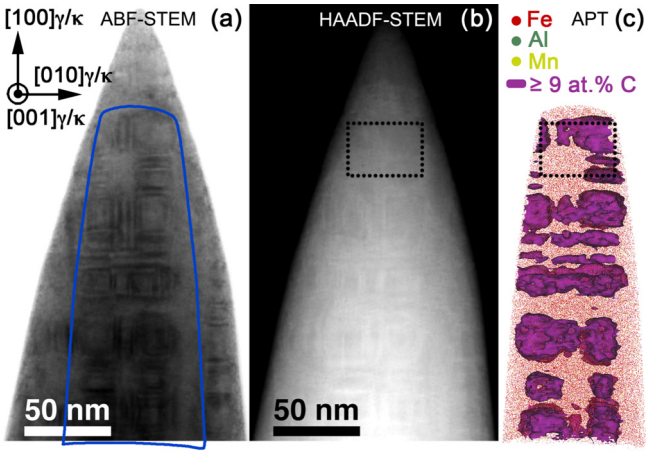

FIG. 1. STEM images of a needle-shaped specimen taken under (a) ABF, (b) HAADF conditions, and corresponding APT reconstruction illustrated in (c). Pronounced contributions from diffraction contrast are present in the ABF image of (a), as seen in the contrast modulations indicating the location of γ/κ interfaces. The perimeter of the APT reconstruction is highlighted in (a). In (b) and (c), the location of direct 1:1 correlation of STEM and APT is indicated.

deliver a fundamental understanding of the atomistic origins of how elastic effects at structurally and chemically complex interfaces affect composition.

II. EXPERIMENTAL DETAILS

The face-centered cubic (fcc) iron (Fe) matrix, referred to as γ-Fe for the remainder of the paper, in low-density steel with a composition of Fe-26.7% Mn-14.0% Al-5.3% C (at. %), is strengthened by nanoscale, coherent κ-carbide precipitates that are formed during the annealing heat treatment at 600 °C (873 K) [23–26]. The detailed processing procedure is described elsewhere [27]. Samples were extracted by focused ion beam (FIB) milling from the bulk and were welded to electropolished Mo half-grids for final sharpening [19]. Before sample extraction, the crystallographic orientation was investigated by electron backscatter diffraction (EBSD) to lift out samples such that $\langle 001 \rangle$ corresponds to the length axis of the APT specimens and electron beam direction in the TEM, respectively. The needle-shaped specimens were first characterized in a C_s-probe corrected FEI Titan Themis 60-300 instrument operated at 300 kV acceleration voltage. Electron probe currents of ∼75 pA were utilized with a semiconvergence angle of 17 mrad. The inner and outer semicollection angles of the annular detectors were chosen to be 7 to 13 mrad for annular bright field (ABF) and 58 to 285 mrad for high angle annular dark field (HAADF). To reduce the influence of scan distortions and instabilities on the obtained atomic resolution STEM images, a serial acquisition scheme of typically 20 images with pixel dwell times of 5 μs was chosen. Consecutive images are aligned and averaged using the nonrigid registration strategy from [12], but with one novel extension. After determining deformations ϕ_i such that the deformed ith frame $f_i \circ \phi_i$ resembles the average f via [12], these deformations are reduced by computing a deformation ψ that minimizes $\sum_{i=1}^{n} \int_\Omega ||\phi_i(\psi(x)) - x||^2 dx$. This way, ψ collects the inverse of the bias, and the bias is removed by replacing ϕ_i with $\phi_i \circ \psi$ and f with $f \circ \psi$. After this additional step, the new average is computed as in [12]. After STEM observations, samples were cleaned with 2 kV Ga^+ ions to remove any contaminants and oxides before each APT measurement. Knowledge of the specimen' s orientation from preceding STEM analysis was used to exploit the partial crystallographic information retained within the APT data, allowing for precise calibration of the reconstruction.

APT data were acquired on a CAMECA LEAP 3000 XR and LEAP 5000 XS in voltage-pulsing mode at ∼70 K with a pulse repetition of 200 kHz, a pulse fraction of 15%, and a target evaporation rate of 5 ions per 1000 pulses, according to the parameters optimized for these samples [27]. The detection efficiency of the former is ∼37% and the latter ∼80%. The collected APT data were reconstructed and analyzed using the commercial software package IVAS (version 3.6.14). By selecting the orientation of the grain from which the specimens are prepared along the $\langle 001 \rangle$, we maximized the chances of detecting atomic planes within the atom probe tomographic reconstruction. A pole was detected in the detector map, as shown in Fig. 2(a), which is the trace of the presence of a set of crystalline planes at the specimen' s surface [28]. This was expected from the atomic arrangement observed from the STEM image (Fig. 1). Within the reconstruction, we made use of the spacing between the imaged planes to calibrate the depth of the reconstruction following the protocol outlined in Ref. [29] and shown in Fig. 2(b), making use of split radial distribution functions known as spatial distribution maps, displayed in Fig. 2(c), to estimate the average spacing between planes [30]. With only a single pole detected, a full calibration of the two main reconstruction parameters could not be performed [31]. The overall depth is calibrated based on the interspacing, and then the image compression factor and field factor were optimized to maximize the flatness of the planes as suggested in the article by Bas *et al.* [32] on which the current generation of reconstruction algorithms is based. In addition, the distortions linked to errors in the reconstruction parameters on relatively small reconstructed volumes, such as the one shown in Fig. 4, are negligible [29,33]. For instance, for the volume shown in Fig. 4, the image compression factor was 1.53 and the field factor 4.7 for an assumed evaporation field of 33 V nm^{-1}. The same approach was used to calibrate the reconstruction shown in Fig. 1.

The theoretical results were obtained using density functional theory (DFT) as implemented in the Vienna Ab Initio Simulation Package (VASP) [34–36]. The electron-ion interaction is described by using projector augmented-wave (PAW) potentials [37,38]. The generalized-gradient approximation (GGA) functional of Perdew, Burke, and Ernzerhof (PBE) [39] was employed. The Methfessel-Paxton method [40] was used for the Fermi surface smearing with a $6 \times 6 \times 6$ Monkhorst-Pack grid [41] in a $2 \times 2 \times 2$ 40-atom supercell (SC) for the κ-carbide and $2 \times 2 \times 2$ 32-atom supercell for the γ-Fe matrix. The single-electron wave functions were expanded by using plane waves up to an energy cutoff of 500 eV. The energies converged to a precision of better than 1 meV/atom. We chose double-layer antiferromagnetic (AFMD) and paramagnetic (PM) states for the γ matrix, whereas ferromagnetic (FM) ordering was chosen for the κ carbide. The PM energies were

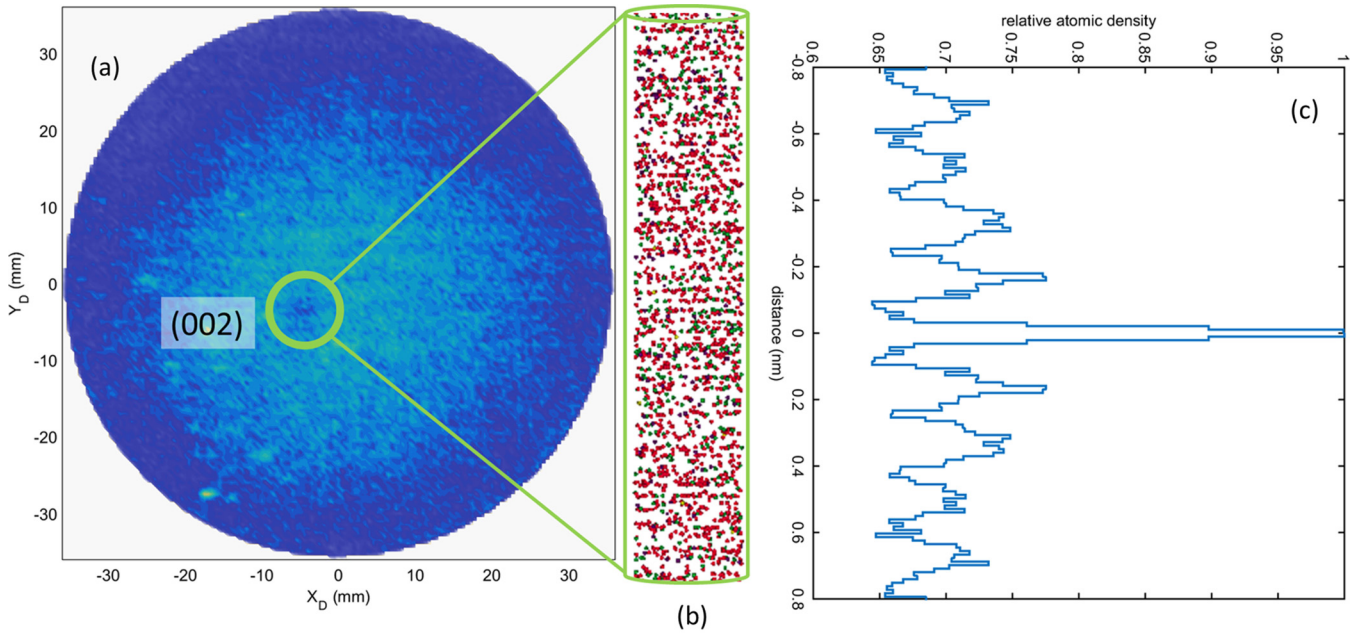

FIG. 2. (a) Two-dimensional detector hit-density histogram for the first 2 million ions acquired during the analysis of the dataset shown in Fig. 4. (b) Atomic planes imaged within the tomographic reconstruction; the color code is similar to that used in Figs. 1 and 4. (c) Spatial distribution map performed during the tomographic reconstruction process enabling the measurement of the average spacing between the (002) planes.

obtained with the aid of the special quasirandom structure (SQS) scheme [42] for a $2 \times 2 \times 2$ SC of γ-Fe. Local relaxations were performed until the forces on each atom were below 0.01 eV/Å for all the magnetic states under consideration.

III. RESULTS AND DISCUSSION

The simultaneously acquired STEM overview images of a representative needle-shaped specimen taken under ABF and HAADF imaging conditions along with the APT reconstruction are shown in Fig. 1. Contributions resulting from diffraction contrast are most pronounced in the ABF image of Fig. 1(a), indicating the localization of strain fields at the matrix-precipitate interfaces. In the HAADF signal of Fig. 1(b) these effects are largely suppressed and the signal mainly represents differences in local composition and thickness. The corresponding reconstructed APT volume is oriented in such a way that the shape of the κ-carbide particles, as defined by the isoconcentration surface for a C concentration of $\geqslant$9 at. %, is corresponding to the observed precipitate structure in the STEM images. The features stemming from strain contrast and the location of γ/κ interfaces agree extremely well when comparing Fig. 1(a) with 1(c). The APT reconstruction now gives access to the 3D shape and distribution of the κ-carbide precipitates, and it can be seen that two types of precipitates, with cuboidal and plate shaped geometry, respectively, are present. The atomic structure of a 3 nm narrow matrix channel separated by two adjacent κ phases is illustrated in Fig. 3. The HAADF-STEM image of Fig. 3(a) clearly confirms the perfect coherency of adjacent κ-carbide precipitates separated by a narrow γ-Fe channel. The color-coded image, based on the nearest-neighbor intensity difference of atomic column peak intensities [Fig. 3(a)], not only highlights the different degree of chemical ordering of both phases but also emphasizes a slight interface roughness of $\sim$1 nm [43].

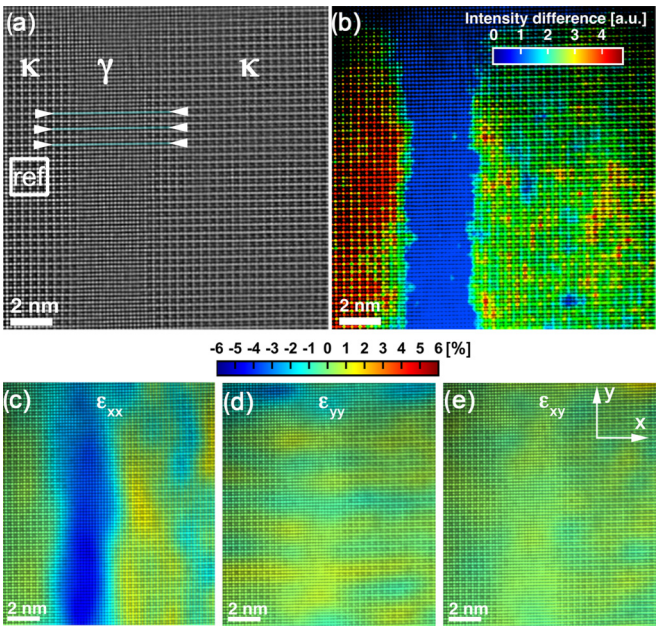

FIG. 3. (a) Fourier-filtered HAADF-STEM image of a narrow γ-Fe matrix channel in between two κ-carbide precipitates. (b) Color coded image of (a) based on the nearest-neighbor intensity difference of atomic columns. A value of 0 indicates the disordered γ-Fe matrix, and values of > 2 represent the chemically ordered κ phase. In-plane strains (c) ε_{xx} and (d) ε_{yy} and shear strain (e) ε_{xy} with respect to a reference region defined in the left κ precipitate. The reference region (ref) for strain determination is indicated in (a).

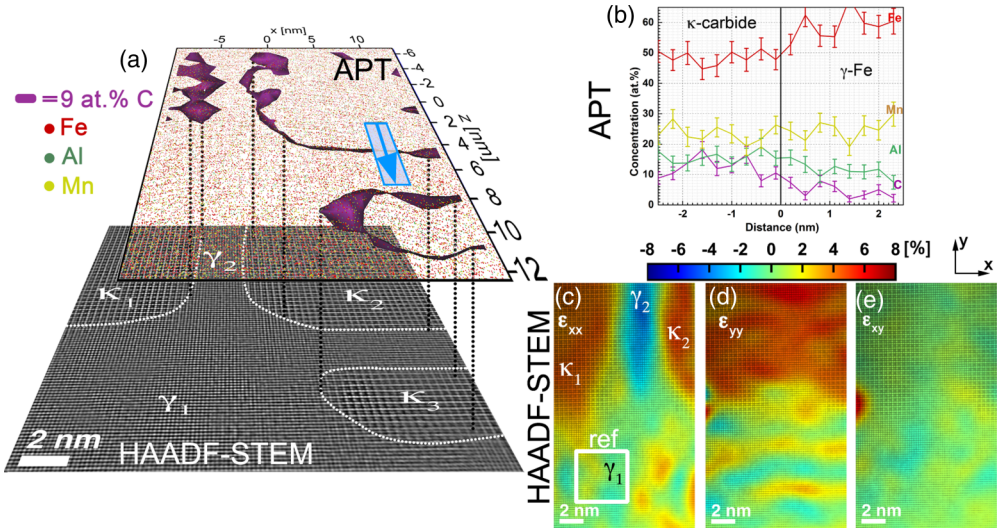

FIG. 4. Direct 1:1 correlation of atomic resolution STEM and APT. The APT reconstruction was refined on the corresponding subvolume using crystallographic information from the detector map and the corresponding structural information from STEM. (a) Superimposed HAADF-STEM image (gray) and APT reconstruction of a 1.5 nm thick slice projected along [001] γ/κ. (b) APT concentration profile extracted across the horizontal γ/κ interface highlighted by the arrow in (a). STEM-deduced in-plane strains (c) ε_{xx} and (d) ε_{yy} and shear strain (e) ε_{xy} with respect to the reference region (ref) defined in the wide γ-Fe matrix channel indicated by the white square.

The local, in-plane strain state across the narrow matrix channel of Fig. 3 a extracted from the atomic column positions is illustrated in Figs. 3(c)–3(e). The atomic column peak positions are refined by fitting them with two-dimensional nonlinear Gaussian functions. A reference region of 2×2 nm^2 was selected in the left κ-carbide phase, that adopts a cubic lattice, to specify a reference lattice as indicated in Fig. 3(a). This reference lattice was then extrapolated to the whole image and the difference between the actual peak positions obtains the displacement field and hence the strain [44]. As expected from this procedure, the normal and shear strain contributions in both κ carbides are $0 \pm 1.5\%$. Interestingly, the strain component perpendicular to the interfaces ε_{xx} [Fig. 3(c)] decreases to -5% compressive strain in the narrow γ-Fe matrix channel. The ratios of the mean, constraint lattice parameters extracted from both adjacent precipitate phases and the matrix phase respectively are $a_{\kappa,x}/a_{\kappa,y} = 1.00$ ($a_{\kappa,x} = 0.379$ nm, $a_{\kappa,y} = 0.379$ nm) and $a_{\gamma,x}/a_{\gamma,y} = 0.95$ ($a_{\gamma,x} = 0.362$ nm, $a_{\gamma,y} = 0.379$ nm), clearly confirming a tetragonal distortion of the narrow γ-Fe channel. The lattice parameter in the plane of the interface ($a_{\parallel}$) expands by 2.6% to retain coherency with adjacent precipitates, while the perpendicular lattice ($a_{\perp}$) is compressed by 2.2% with respect to the cubic lattice of a broad matrix channel [γ_1 in Fig. 4(a)] with $a_{\gamma_1,x} = 0.370$ nm, $a_{\gamma_1,y} = 0.369$ nm.

These results were obtained in a region very close to the apex of the needle-shaped specimen, that is difficult to conserve in APT measurements. In a slightly thicker specimen region, both structural and compositional information were obtained from STEM imaging and subsequent correlative APT measurements, illustrated in Fig. 4. The superposition of the HAADF-STEM image agrees well with the corresponding APT reconstruction, as seen in Fig. 4(a). Here, a thin slice of the APT reconstruction is oriented in such a way as to correspond to the viewing direction of [001] in the STEM experiments. Since in this case the APT data iare plotted from an inclined perspective, an additional movie revealing the 3D topology of this region is given in the Supplemental Material [45]. The compositional gradients across the interface of a narrow matrix channel extend over ~2–3 nm with a decrease in C concentration from 12 at. % in κ to 5 at. % in γ, illustrated in Fig. 4(b). The complex strain state that evolves in the transition region of broad (γ_1) and narrow (γ_2) matrix channels indicates that local lattice distortions, as seen in Figs. 4(c)–4(e), play an important role in understanding solute distribution.

DFT calculations, in combination with thermodynamic concepts, are employed to explore the impact of tetragonal lattice distortions of γ-Fe on C solubility. A detailed description of the basic methodology is given in Ref. [22]. The tetragonal strain is defined in agreement with experiments as $\varepsilon = (a_{\perp} - a_{\parallel})/a_{\parallel}$, with $a_{\perp}$ as the lattice parameter of γ perpendicular to the γ/κ interface and $a_{\parallel}$ in plane with the γ/κ interface. For both AFMD and PM calculations the C solution enthalpy is observed to increase with a decrease in imposed tetragonal strain, as illustrated in Fig. 5(a).

This trend suggests that the experimentally obtained tetragonal strain of -5% in the narrow matrix channels leads to an increase in C solubility with respect to the broad channels ($\varepsilon = 0\%$). The comparison of AFMD and PM was chosen because the magnetic low-temperature state of γ-Fe is AFMD, which by itself favors a tetragonal distortion of the cubic lattice [vertical arrow in Fig. 5(a)] [46,47]. The PM case gives a more realistic representation of the magnetic state at the annealing temperature of 873 K. Furthermore, the results show that this qualitative trend is independent of the magnetic state and does not change by increasing the C concentration. Absolute values of solution enthalpy depend on the chemical potential that is determined by the chemical equilibrium between γ and κ. Thus, the partitioning of C atoms between hydrostatically strained κ carbide and biaxially strained γ is determined by an energy minimization scheme where chemical and elastic energies of both phases are considered along with

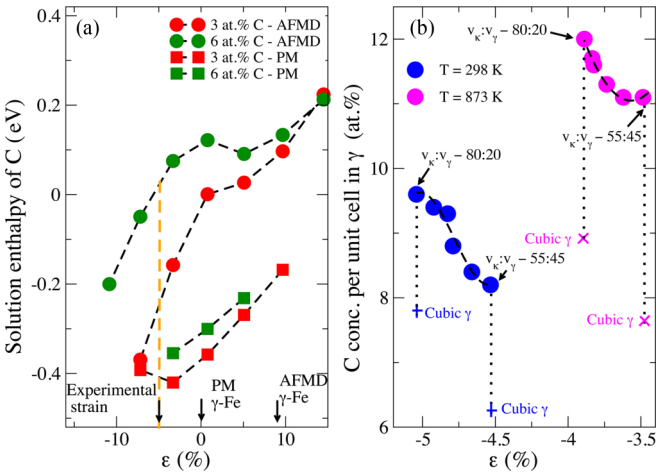

FIG. 5. (a) Solution enthalpy for two C concentrations in γ-Fe computed at fixed volumes as a function of imposed tetragonal strain for AFMD (double-layer antiferromagnetic) and PM (paramagnetic) states. The tetragonal strain present in the experiment, for AFMD and PM γ-Fe, is indicated by vertical arrows. (b) C concentration in γ-Fe as a function of tetragonal strain at 298 and 873 K. Here, the γ-Fe matrix is treated in the AFMD state. The pluses and crosses indicate values resembling the broad, cubic γ channels. $v_\kappa : v_\gamma$ is the volume fraction ratio of κ and γ.

configurational entropy contributions [22]. This situation is chosen to represent the experimentally observed lattice configurations of κ and γ. In these calculations, the tetragonal strain is not a free parameter but is imposed by the relative weight of κ and γ in the elastic energy contribution, represented by the volume fractions of both phases v_κ and v_γ, respectively. The tetragonal strain values determined at room temperature (298 K) are in excellent agreement with the experimental results shown in Fig. 3. The C concentration in γ-Fe is seen to increase by $\sim$1.8 at. % from -4.5% to -5% tetragonal strain at 298 K, as shown in Fig. 5(b). A similar trend is observed at 873 K with an increase of the C concentration from 11 to 12 at. %. This indicates that narrow γ-Fe channels are supersaturated with C by a factor of 2 or more, with respect to solubility limits obtained in similar alloy systems [48]. At the same time, the tetragonal strain is reduced to values between -3.5% and -4% at 873 K. This suggests that temperature affects the partitioning of C between κ and γ, and also the strain state. The observed increase in C concentration in γ is fully consistent with the previously calculated C solution enthalpy [Fig. 5(a)], and a similar behavior is expected for C partitioning between κ and γ for PM γ-Fe. The impact on the C concentration for hydrostatically strained γ is highlighted by plus and cross symbols at 298 and 873 K for two choices of volume fraction of κ and γ, respectively, in Fig. 5(b). For both temperatures, a decrease in C concentration of $\sim$2 at. % at 298 K and $\sim$3 at. % at 873 K can be confirmed, verifying that tetragonally strained γ can dissolve larger amounts of C. These compositional differences are not detected by APT, which is a state-of-the-art technique to resolve nanometer-scale compositional gradients of light elements in a heavy matrix. However, deviations in the field evaporation behavior of the different phases lead to ion trajectory aberrations, which are known to compromise the accuracy of atom probe reconstructions [27,28].

IV. CONCLUSIONS

In conclusion, by interlinking quantitative atomic resolution STEM, APT, and DFT, the connection of complex elastic strain fields at interfaces with local impurity concentrations is established with highest lateral resolution and chemical sensitivity. The structural information from STEM provides insights into the complex strain state across coherent γ/κ interfaces, and a tetragonal distortion of nanometer-sized γ-Fe channels is found. APT determines the concentration of C in γ-Fe around the precipitates to $\sim$5 at. %, but compositional differences in the broad and narrow channels are not detectable. The experimentally informed DFT calculations, however, establish that an increasing tetragonal strain leads to an increase in C concentration. This could also explain the experimentally observed broad C concentration gradient across the interface, since the first atomic layers of γ in proximity to the interfaces are under highest strain, that partly relaxes when moving away from the interface.

The computed increase in C concentration in the narrow, tetragonal channels indicates a supersaturation of γ-Fe with C by a factor of 2 or more, in comparison to values obtained from equilibrium phase diagrams. Hence, it is expected that these channels contribute to strengthening by impeding dislocation mobility and affect phase stability by an increase in C diffusivity.

ACKNOWLEDGMENTS

The authors are very thankful for fruitful discussions with D. Ponge. Financial support by the Deutsche Forschungsgemeinschaft (DFG) within SFB761 "steel ab initio" is acknowledged.

[1] N. Nakagawa, H. Y. Hwang, and D. A. Muller, Nat. Mater. **5**, 204 (2006).
[2] K. Lu, L. Lu, and S. Suresh, Science **324**, 349 (2009).
[3] G. Gottstein, *Physical Foundations of Materials Science*, 1st ed. (Springer, Berlin, 2004).
[4] J. Dundurs and T. Mura, J. Mech. Phys. Solids **12**, 177 (1964).
[5] D. J. Srolovitz, M. J. Luton, R. Petkovic-Luton, D. M. Barnett, and W. D. Nix, Acta Metall. **32**, 1079 (1984).
[6] P. W. Voorhees, J. Stat. Phys. **38**, 231 (1985).
[7] W. C. Johnson and P. W. Voorhees, J. Appl. Phys. **61**, 1610 (1987).
[8] A. J. Ardell and V. Ozolins, Nat. Mater. **4**, 309 (2005).
[9] *Scanning Transmission Electron Microscopy*, edited by S. J. Pennycook and P. D. Nellist (Springer, Berlin, 2011).
[10] D. N. Seidman, Annu. Rev. Mater. Res. **37**, 127 (2007).
[11] P. E. Batson, N. Dellby, and O. L. Krivanek, Nature (London) **418**, 617 (2002).
[12] B. Berkels, P. Binev, D. A. Blom, W. Dahmen, R. C. Sharpley, and T. Vogt, Ultramicroscopy **138**, 46 (2014).

[13] A. B. Yankovich, B. Berkels, W. Dahmen, P. Binev, S. I. Sanchez, S. A. Bradley, A. Li, I. Szlufarska, and P. M. Voyles, Nat. Commun. **5**, 1 (2014).
[14] L. Jones, S. Wenner, M. Nord, P. H. Ninive, O. M. Løvvik, R. Holmestad, and P. D. Nellist, Ultramicroscopy **179**, 57 (2017).
[15] D. Larson, B. Gault, B. Geiser, F. D. Geuser, and F. Vurpillot, Curr. Opin. Solid State Mater. Sci. **17**, 236 (2013).
[16] I. Arslan, E. A. Marquis, M. Homer, M. A. Hekmaty, and N. C. Bartelt, Ultramicroscopy **108**, 1579 (2008).
[17] S. I. Baik, X. Yin, and D. N. Seidman, Scr. Mater. **68**, 909 (2013).
[18] M. Herbig, D. Raabe, Y. J. Li, P. Choi, S. Zaefferer, and S. Goto, Phys. Rev. Lett. **112**, 126103 (2014).
[19] M. Herbig, P. Choi, and D. Raabe, Ultramicroscopy **153**, 32 (2015).
[20] W. Lefebvre, D. Hernandez-Maldonado, F. Moyon, F. Cuvilly, C. Vaudolon, D. Shinde, and F. Vurpillot, Ultramicroscopy **159**, 403 (2015).
[21] J. Neugebauer and T. Hickel, Wiley Interdiscip. Rev. Comput. Mol. Sci. **3**, 438 (2013).
[22] P. Dey, R. Nazarov, B. Dutta, M. Yao, M. Herbig, M. Friák, T. Hickel, D. Raabe, and J. Neugebauer, Phys. Rev. B **95**, 104108 (2017).
[23] G. Frommeyer and U. Brüx, Steel Res. Int. **77**, 627 (2006).
[24] K. M. Chang, C. G. Chao, and T. F. Liu, Scr. Mater. **63**, 162 (2010).
[25] H. Springer and D. Raabe, Acta Mater. **60**, 4950 (2012).
[26] I. Gutierrez-Urrutia and D. Raabe, Mater. Sci. Technol. **30**, 1099 (2014).
[27] M. J. Yao, P. Dey, J. B. Seol, P. Choi, M. Herbig, R. K. W. Marceau, T. Hickel, J. Neugebauer, and D. Raabe, Acta Mater. **106**, 229 (2016).
[28] B. Gault, M. P. Moody, J. M. Cairney, and S. P. Ringer, *Atom Probe Microscopy*, Springer Series in Materials Science Vol. 160 (Springer, Berlin, 2012).
[29] B. Gault, M. Moody, F. De Geuser, G. Tsafnat, A. La Fontaine, L. Stephenson, D. Haley, and S. Ringer, J. Appl. Phys. **105**, 034913 (2009).
[30] B. P. Geiser, T. F. Kelly, D. J. Larson, J. Schneir, and J. P. Roberts, Microsc. Microanal. **13**, 437 (2007).
[31] B. Gault, F. de Geuser, L. T. Stephenson, M. P. Moody, B. C. Muddle, and S. P. Ringer, Microsc. Microanal. **14**, 296 (2008).
[32] P. Bas, A. Bostel, B. Deconihout, and D. Blavette, Appl. Surf. Sci. **87-88**, 298 (1995).
[33] B. Gault, S. T. Loi, V. J. Araullo-Peters, L. T. Stephenson, M. P. Moody, S. L. Shrestha, R. K. W. Marceau, L. Yao, J. M. Cairney, and S. P. Ringer, Ultramicroscopy **111**, 1619 (2011).
[34] G. Kresse and J. Hafner, Phys. Rev. B **48**, 13115 (1993).
[35] G. Kresse and J. Furthmüller, Phys. Rev. B **54**, 11169 (1996).
[36] G. Kresse and J. Furthmüller, Comput. Mater. Sci. **6**, 15 (1996).
[37] P. Blöchl, Phys. Rev. B **50**, 17953 (1994).
[38] G. Kresse and D. Joubert, Phys. Rev. B **59**, 1758 (1999).
[39] J. Perdew, K. Burke, and M. Ernzerhof, Phys. Rev. Lett. **77**, 3865 (1996).
[40] M. Methfessel and A. T. Paxton, Phys. Rev. B **40**, 3616 (1989).
[41] J. D. Pack and H. J. Monkhorst, Phys. Rev. B **16**, 1748 (1977).
[42] A. Zunger, S.-H. Wei, L. G. Ferreira, and J. E. Bernard, Phys. Rev. Lett. **65**, 353 (1990).
[43] C. H. Liebscher, V. R. Radmilovic, U. Dahmen, N. Q. Vo, D. C. Dunand, M. Asta, and G. Ghosh, Acta Mater. **92**, 220 (2015).
[44] M. J. Hÿtch, E. Snoeck, and R. Kilaas, Ultramicroscopy **74**, 131 (1998).
[45] See Supplemental Material at http://link.aps.org/supplemental/10.1103/PhysRevMaterials.2.023804 for movie of 3D-APT reconstruction.
[46] D. W. Boukhvalov, Y. N. Gornostyrev, M. I. Katsnelson, and A. I. Lichtenstein, Phys. Rev. Lett. **99**, 247205 (2007).
[47] N. I. Medvedeva, D. Van Aken, and J. E. Medvedeva, J. Phys.: Condens. Matter **22**, 316002 (2010).
[48] K. Ishida, H. Ohtani, N. Satoh, R. Kainuma, and T. Nishizawa, ISIJ Int. **30**, 680 (1990).